

X27A—A new hard X-ray micro-spectroscopy facility at the National Synchrotron Light Source

J.M. Ablett^{a,*}, C.C. Kao^a, R.J. Reeder^b, Y. Tang^b, A. Lanzirotti^c

^a*National Synchrotron Light Source, Brookhaven National Laboratory, Upton, NY 11973, USA*

^b*Department of Geosciences and Center for Environmental Molecular Science, State University of New York at Stony Brook, Stony Brook, NY 11794-2100, USA*

^c*Consortium for Advanced Radiation Sources, University of Chicago, Chicago, ILL 60637, USA*

Received 29 December 2005; received in revised form 8 February 2006; accepted 9 February 2006

Available online 20 March 2006

Abstract

A new hard X-ray micro-spectroscopy beamline has recently been installed at bending-magnet beamline X27A at the National Synchrotron Light Source, where the focus of research is primarily directed towards the environmental, geological and materials science communities. This instrument delivers moderate, $\sim 10\mu\text{m}$ spatial resolution using achromatic dynamically bent Kirkpatrick–Baez mirrors, in addition to providing high X-ray flux throughput and selectable energy resolution. The balance between moderate spatial resolution and high flux throughput, in combination with a liquid nitrogen-cooled 13-element energy-dispersive high-purity germanium detector, is particularly well suited to the investigation of dilute and thin-film systems using the fluorescence X-ray absorption fine-structure mode of detection. In this paper, we report on the design and performance of this instrument and highlight a recent experimental study undertaken at this facility.

© 2006 Elsevier B.V. All rights reserved.

1. Introduction

Processes that occur on the micron and nanometer length scales ultimately determine the macroscopic properties of a system and are a rich area for investigation. For this reason, hard X-ray ($\sim > 3\text{ keV}$) micro/nano-probes are in high demand at synchrotron radiation facilities. These instruments have the ability of obtaining spatially resolved electronic and structural information through spectroscopic and diffraction-based techniques using a variety of X-ray focusing elements [1,2]. The X27A micro-spectroscopy beamline at the National Synchrotron Light Source (NSLS) will provide access across a wide range of scientific disciplines, with a particular emphasis on environmental science. The application of X-ray microprobes in environmental studies is becoming increasingly popular among the academic and industrial research communities [3–9]. For example, the understanding of the role of metal contamination in soils and plants is important in determining the

overall ecological impact of the pollutants and developing successful remediation strategies. X-ray micro-spectroscopy can reveal the heterogeneity and identify the speciation and association of the various contaminants, and thus can supply key information on the toxicity, mobility and their overall fate in the surroundings.

At NSLS X27A, the X-rays are achromatically micro-focused onto the sample using dynamically bent rhodium-coated Kirkpatrick–Baez (KB) mirrors. The full-width-half maximum (FWHM) focused X-ray beam size is $\sim 6\mu\text{m}$ [vertical] $\times 17\mu\text{m}$ [horizontal]. The energy range from ~ 4 to 32 keV can be accessed through a combination of silicon (111) and (311) channel-cut monochromators. The sample under investigation is mounted on motorized (sub-micron resolution) translation and rotation stages and raster-scanned through the micro-focused X-ray beam. Fluorescence is measured using a liquid-nitrogen cooled 13-element energy-dispersive high-purity germanium detector, and the sample is scanned in a ‘step-and-repeat’ mode. Two-dimensional elemental compositional maps, X-ray absorption near-edge structure (XANES) and extended X-ray absorption fine-structure (EXAFS) studies

*Corresponding author. Tel.: +6313444435; fax: +6313443238.

E-mail address: jablett@bnl.gov (J.M. Ablett).

can be performed at this beamline with $\sim 10\ \mu\text{m}$ spatial resolution. The following sections describe the design and operation of the NSLS X27A micro-spectroscopy facility.

2. X27A source, beamline and monochromator

The X27A microprobe end-station is located approximately 10.8 m from the dipole bending-magnet port (6-mrad opening angle) on the NSLS 2.8 GeV X-ray storage ring. This particular port was chosen to host the new X27A microprobe end-station because the closer proximity to the source, compared with longer beamlines at the NSLS, delivers higher X-ray flux to the sample. The source parameters are tabulated in Fig. 1a, and a plot of the calculated X-ray flux through a $1\ \text{mm} \times 1\ \text{mm}$ aperture within the X27A experimental hutch, taking into account absorption through the two beryllium windows in the beamline, is shown in Fig. 1b. By considering the X-ray energy, the grazing-incidence angles of the KB optics, the channel-cut monochromator being used, and the X-ray absorption through the experimental air path, this plot can be conveniently used to calculate the X-ray intensity at the sample location (Section 3).

Fig. 2 shows the elevation layout of the X27A beamline components; a valve, a pump-out port, a beryllium window (A), a set of slits (B) and monochromator (C), a secondary beryllium window (D), the X27A experimental end-station and a Pb beam-stop (E). A lead shutter, located upstream of the concrete shield wall, allows the synchrotron radiation to propagate along the evacuated beam pipe (pressure less than 3×10^{-9} Torr) and into the experimental hutch. There are two beryllium windows ($254\ \mu\text{m}$ thick, ultrahigh-purity grade) within the X27A beamline at locations A and D in Fig. 2, and the window at A is water cooled. The photon beam dimensions are defined at the monochromator location (C) using motorized four-jaw water-cooled tungsten blades (B). The experimental end-station is shown within the experimental hutch (the line at 10.890 m indicates the center of the vertical focusing mirror of the KB system), and a lead beam-stop is situated at 12.250 m from the source.

The X27A beamline incorporates a side-by-side arrangement of 1 cm wide channel-cut crystals [silicon (1 1 1) and silicon (3 1 1)] separated by 1 cm wide gap, as shown in Fig. 3. The fan of synchrotron radiation at the monochromator position (9.2 m from the source) is approximately 5 cm wide and sufficient to illuminate the entire crystal assembly. For this reason, the X27A facility was designed so that the experimental end-station is translated laterally to match the crystal of choice, while the monochromator crystals themselves remain fixed in position and can only rotate. The crystals are mounted on a water-cooled copper block and an indium–gallium eutectic between them ensures good thermal coupling. The channel-cut crystals are mounted on a 360° rotation stage and follow the standard NSLS monolithic-elastic design [10,11], which provides for a simple, cost-effective and robust

Electron Energy	2.8 GeV
Average Electron Current	235 mA
Bending Magnet Radius	6.875 m
Bending Magnet Field	1.36 T
Critical Energy	7.091 keV
Horizontal Emittance	68 nm rad
Coupling Constant	0.002
Natural Energy Spread	0.00092
Horizontal Source Size (rms)	$410.0\ \mu\text{m}$
Vertical Source Size (rms)	$68.0\ \mu\text{m}$
Horizontal Source Divergence (rms)	$390\ \mu\text{rad}$
Vertical Source Divergence (rms)	$13.2\ \mu\text{rad}$

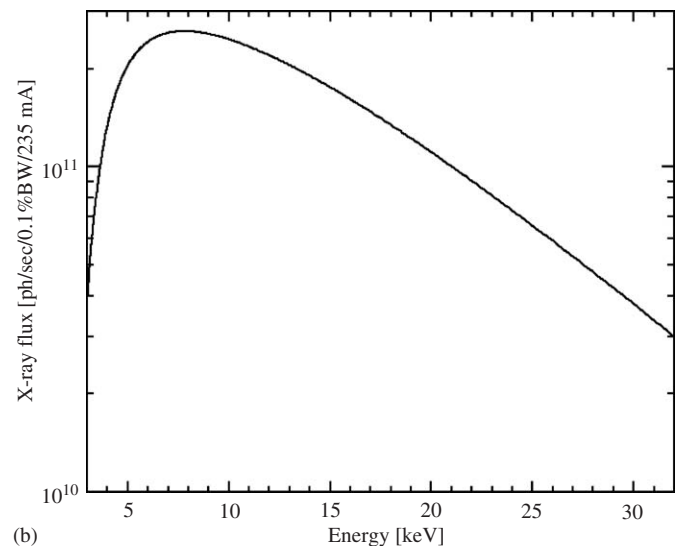


Fig. 1. (a) X27A electron source parameters. (b) Calculated X-ray flux through an on-axis $1\ \text{mm} \times 1\ \text{mm}$ aperture within the X27A experimental hutch, including absorption through the two beamline beryllium windows.

monochromator system. The silicon (1 1 1) and silicon (3 1 1) crystals, with channel-cut gaps of 6 and 7 mm, respectively, can span the energy range from ~ 3.8 up to 32 keV, thus providing access to the K and L absorption edges of most of the periodic table. Detuning of the crystals is accomplished through piezoelectric-driven actuators that are in contact with the upper crystal blocks, and a third actuator is used for adjusting the yaw of the setup with respect to the incident X-ray beam. The overall energy resolution is in principle determined by a combination of both the intrinsic Darwin width of the crystal ($[dE/E] \sim 1.4 \times 10^{-4}$ and 2.9×10^{-5} for the silicon (1 1 1) and (3 1 1) reflections, respectively), the angular divergence of the photon beam on the crystal, and the natural line widths of the X-ray transition levels involved in the measurement. The calculated instrumental energy resolutions (FWHM) of the X27A monochromator in the appropriate range of

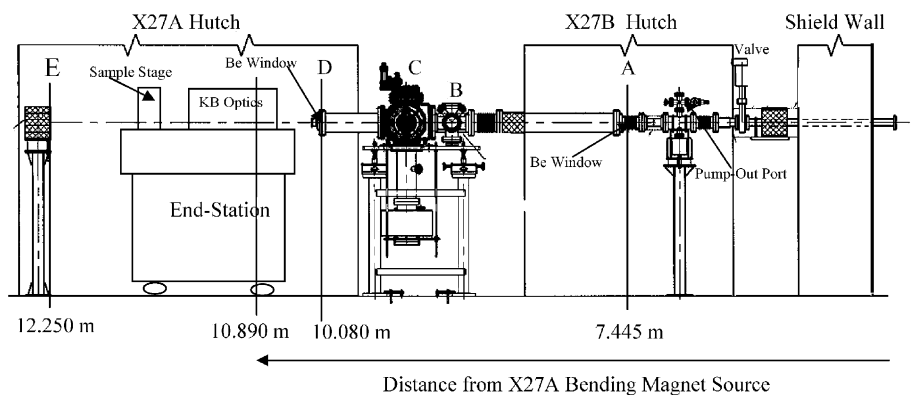


Fig. 2. Elevation layout of the X27A beamline components. Distances are given from the X27A dipole bending magnet port.

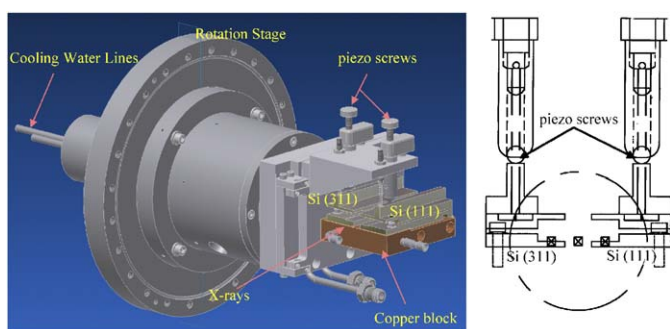


Fig. 3. Schematic of the X27A monochromator crystal arrangement and associated components.

operation for each of the crystal pairs are listed in Table 1. There are three columns in Table 1 for both the silicon (111) and (311) crystals; the intrinsic energy resolution (ΔE_i), and the actual instrumental energy resolution for vertical slit settings of 0.5 mm ($\Delta E_{1/2}$) and 1.0 mm (ΔE_1). In addition, natural lifetime broadenings of selective K and L absorption edges are included in Table 1 [12,13]. The combination of Si(111) and Si(311) monochromators, and the adjustable monochromator slits, allow for the instrumental energy resolution to be smaller than the natural line-widths of the transitions under investigation. The instrumental resolution that is calculated in Table 1, can be experimentally inferred from measurements taken at narrow absorption-edge features from various standards that are available at the X27A beamline. If required, the instrumental resolution can be lowered, but with a corresponding reduction in X-ray intensity, by reducing the vertical slit size of the motorized 4-jaw slit assembly (Fig. 2).

3. X27A end-station, optics and detectors

A top-view schematic of the X27A experimental end-station layout is shown in Fig. 4. Monochromatic X-rays enter the X27A experimental hutch through a beryllium window and propagate along a 65 cm flight path. Although

the acceptance of the KB optics ($\leq 1 \text{ mm}^2$) is sufficient to select only the required Bragg-diffracted beam from the channel-cut monochromator, a lead slit ($\sim 1.5 \text{ mm} \times 1.5 \text{ mm}$) is situated immediately downstream of the flight path to absorb unwanted reflections emanating from the crystals. In fact, most of these extraneous reflections are stopped immediately after the crystals by the copper beamstop in the monochromator tank. After passing through the lead slit, the X-rays then transverse a 1 cm long ionization chamber before entering the micro-focusing mirror enclosure. Helium gas is flowed through both the flight path and mirror enclosure to eliminate absorbance of the X-rays in air. The micro-focusing mirrors are a rhodium-coated KB pair that are clamped within a motorized bender system, and can be accurately aligned with respect to the incident X-ray beam [14]. This mechanism is adjusted to form the required elliptical shape for micro-focusing the incoming X-rays at the sample location. The X27A micro-focusing mirrors themselves consist of 20 cm long (17.2 cm useable mirror length) trapezoidal-shaped single-crystal silicon substrates that are polished to a roughness better than 1 \AA rms (root-mean-square). An $\sim 50 \text{ \AA}$ binding layer of chromium is deposited onto these substrates, followed by an $\sim 500 \text{ \AA}$ layer of rhodium, which acts as the X-ray reflecting surface. As the horizontal source size of the electron beam is much larger than that in the vertical direction (Fig. 1a), the horizontal focusing mirror is placed downstream from that of the vertical focusing optic to achieve a greater demagnification of the source size in this direction. The X-rays are focused at a distance of 9 cm from the end of the mirror enclosure, to a FWHM spot size of $\sim 6 \mu\text{m}$ [vertical] $\times 17 \mu\text{m}$ [horizontal]. Another 1 cm long ionization chamber is used to monitor the X-ray intensity just before the sample, for normalization purposes. Depending upon the X-ray energy range in use, sufficient signal is obtained from these small-length ionization chambers by flowing appropriate gases through them.

The optical parameters for the X27A micro-focusing optics are detailed in Table 2. Depending upon the X-ray energy, the grazing-incidence angles of the mirrors are adjusted to achieve total external reflection. For appreciable reflectivity (e.g. 80% for a single surface, 64% for the

Table 1
Calculated instrumental energy resolution (FWHM) of the X27A silicon (1 1 1) and silicon (3 1 1) monochromators

E (keV)	Si (1 1 1)			Si (3 1 1)			Natural level widths	
	ΔE_i (eV)	$\Delta E_{1/2}$ (eV)	ΔE_1 (eV)	ΔE_i (eV)	$\Delta E_{1/2}$ (eV)	ΔE_i (eV)	Core level	E_f (eV)
4	0.57	0.70	0.96	—	—	—	Ca (K)	0.81
5	0.73	0.96	1.46	—	—	—	Ti (K)	0.94
6	0.87	1.27	2.05	0.17	0.43	0.82	Pr (L_3)	3.60
7	1.01	1.63	2.75	0.20	0.62	1.20	Fe (K)	1.25
8	1.15	2.04	3.57	0.23	0.83	1.62	Ho (L_3)	4.26
10	1.42	3.03	5.54	0.29	1.35	2.66	W (L_3)	4.98
15	2.12	6.46	12.38	0.42	3.14	6.23	Rb (K)	4.44
17	2.83	7.84	15.68	0.48	4.02	8.04	U (L_3)	7.43
20	2.82	11.24	21.94	0.56	5.63	11.22	Mo (K)	4.52
25	—	—	—	0.70	8.84	17.63	Ag (K)	6.75
30	—	—	—	0.84	12.76	25.48	Sb (K)	9.16

The values shown are the incident X-ray energy E , the intrinsic resolution (ΔE_i) and the actual instrumental energy resolution due to the X-ray beam divergence through a 0.5 mm ($\Delta E_{1/2}$) and a 1 mm (ΔE_1) vertical slit opening. Also shown are selected core-level energy broadenings (FWHM), E_f [12,13].

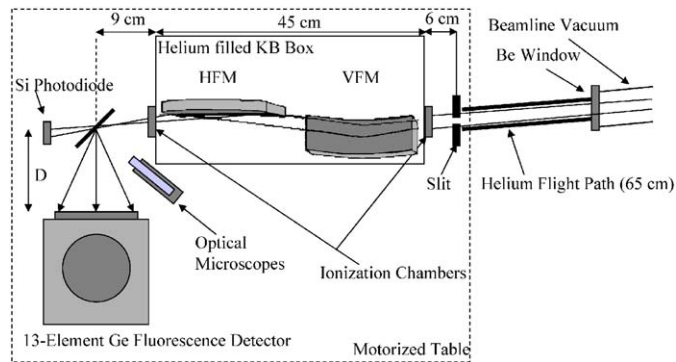


Fig. 4. Top-view schematic of the X27A microprobe end-station. VFM and HFM are the vertical and horizontal focusing KB mirrors, respectively. The sample is viewed using optical microscopes and the transmitted X-rays are detected using a silicon photodiode. Fluorescence X-rays are collected with the 13-element liquid nitrogen-cooled germanium detector. The distance from the sample to this detector, D is varied using a motorized linear slide. There is a total experimental air path (between beryllium window and sample location) of 15 cm.

KB pair) and acceptance, the angles of incidence are around 5 mrad (4 → 12 keV), 3.5 mrad (12 → 18 keV), 2.6 mrad (18 → 23 keV) and 1.9 mrad (23 → 30 keV), translating into acceptances of $860 \times 860 \mu\text{m}^2$, $602 \times 602 \mu\text{m}^2$, $447 \times 447 \mu\text{m}^2$ and $327 \times 327 \mu\text{m}^2$, respectively. The energy-dependent X-ray intensity on the sample at X27A can then be estimated by combining the following; the X-ray flux values plotted in Fig. 1b, the reflectivity of each of the KB mirrors, the vertical and horizontal mirror acceptances (in mm), the intrinsic band-pass of the silicon (1 1 1) or (3 1 1) crystal in units of 0.1% bandwidth, the crystal reflectivity and lastly, the absorption of X-rays through the 15 cm experimental air path. Using the grazing incidence angles for a combined 64% KB reflectivity as previously stated, the calculated X-ray flux at 4, 10, 15 and 20 keV for the silicon (1 1 1) monochromator are 1.2×10^9 , 1.3×10^{10} , 5.2×10^9 and 1.8×10^9 ph/s respectively. For the silicon (3 1 1) monochromator, the calculated X-ray flux at 5.5, 10,

Table 2
X27A optical parameters

X27A micro-focusing optical parameters	VFM	HFM
Source-to-mirror pole distance	10.89 m	11.10 m
Focal length	42 cm	21 cm
Demagnification	26:1	53:1
Perfect image size (FWHM)	6.2 μm	18.2 μm
Estimated image size (FWHM)	6.9 μm	18.2 μm
Spatial acceptance	602 μm	602 μm
Angular acceptance	55.3 μrad	54.2 μrad
Photon beam divergence	1.4 mrad	2.9 mrad

VFM and HFM are the vertical and horizontal focusing KB mirrors, respectively. The estimated image size is based on a $1.5 \mu\text{rad}$ rms figure error of the KB optical surfaces. The acceptance and divergence of the KB arrangement assumes a 3.5 mrad grazing incidence angle and a 17.2 cm useable mirror surface.

15, 20, 25 and 30 keV are 1.2×10^9 , 2.7×10^9 , 1.1×10^9 , 3.8×10^8 , 1.3×10^8 and 7.3×10^7 ph/s respectively. The X27A experimental end-station is aligned by monitoring the ionization signals on both the front and rear of the mirror enclosure, and by viewing the focused X-ray beam on a scintillator crystal (Section 5). Detuning of the monochromator crystals is performed prior to data collection to significantly reduce higher-order harmonic content from entering the experimental hutch. Measurements of the X-ray flux at the sample position are continuously recorded during an experiment using the ionization chambers and/or silicon photodiode, and are found to be around 20% lower than the calculated values.

The sample is typically orientated normal to the direction of X-ray propagation and at a 45° horizontal incidence angle. The liquid-nitrogen cooled 13-element germanium fluorescence detector is located in the horizontal plane of the synchrotron ring and at 90° to the X-ray beam direction, thus reducing elastically scattered radiation from entering the detector. Each of the detector elements is circular with a diameter of 1 cm. The detector is

mounted on a motorized linear slide that allows the detector–sample distance to be adjusted. The detector system employs digital processing electronics, and a FWHM energy resolution at 5.895 keV of ~ 180 eV is measured for a shaping time of 6 μ s (averaged over the whole detector array). With a shaping time of 1 μ s, the detector can easily be run at input count rates exceeding 5×10^4 cps per detector element, with a corresponding FWHM energy resolution at 5.895 keV of ~ 260 eV. X-ray transmission can also be performed at X27A by utilizing the silicon photodiode that is located downstream of the sample location.

The end-station, which sits upon vibrational damping air pads, is housed upon a motorized 6-axis experimental honeycomb table, thus allowing the whole assembly to be positioned vertically, to optimize for a particular energy range of interest, or translated laterally to intercept silicon (111) or (311) monochromatic radiation. As the monochromator design is not fixed exit, the vertical height of the X-ray beam emerging from the crystals changes as the X-ray energy is varied. The vertical displacement of the output beam with respect to the incident synchrotron white beam is equal to twice the crystal gap multiplied by the cosine of the crystal angle, and is thus more pronounced at lower X-ray energies. This beam motion is equivalent to a source motion, and thus the micro-focused X-ray beam also moves on the sample as the energy is scanned, but by a reduced amount due to the vertical demagnification of the KB optics. However, this motion is typically well within the envelope of the focused spot size itself, especially in XANES measurements which have a very limited energy range (typically 200 eV or less) and is therefore not a major concern. However, in EXAFS measurements, the scan range can exceed 1 keV and the change in vertical beam displacement should be considered. For example, using the silicon (111) monochromator and scanning from 8 to 9.5 keV, the vertical beam exiting the monochromator changes by ~ 109 μ m. The demagnification in the vertical direction is 26:1 (Table 2) and thus the focused spot size moves vertically upwards on the sample by 4 μ m. For lower X-ray energy ranges these displacements increase, and the motorized experimental table is adjusted to compensate for this beam motion. This is accomplished by dividing the energy scan range into sections, the number of which are determined through consideration of the focused beam motion. After completion of a particular energy scan section, the experimental table is correspondingly raised or lowered to match the focused beam position on the sample, and the subsequent scan section is performed. In this way, the experimental table is not continuously scanned but adjusted only when beam motion becomes significant (e.g. 50% of the vertical focused beam size).

4. X-ray beam profile measurements

For accurately determining the X27A micro-focused X-ray beam profile, a patterned silicon substrate consisting

of an array of 1 μ m diameter 1500 \AA thick nickel dots, each separated by a distance of 50 μ m, was utilized. First of all, a 5 μ m thin YAG:Ce scintillator crystal (Crytur Ltd, Czech Republic) deposited on a glass substrate was mounted on the sample stage and positioned within the focused X-ray beam. An incident energy of 9 keV using the silicon (111) monochromator was selected, above the Ni K-absorption edge, and a region of interest was set around the Ni fluorescence line (7.472 keV) on the multi-channel analyzer. The visible light emanating from the thin scintillator was then viewed using a high-magnification ($10\times$) optical microscope with a depth of focus of ~ 3.5 μ m, and the mirror benders adjusted until the best focused X-ray spot size was obtained. A view of this image, as captured by a frame grabber, is shown in Fig. 5b. In the normal operating geometry at X27A, and used during this measurement, the sample was placed at a 45° angle to the direction of X-ray incidence in the horizontal plane (see Fig. 4.), and consequently the footprint of the X-ray beam on the sample is larger by a factor of $\sqrt{2}$ compared with normal incidence operations. The nickel $K\alpha$ fluorescence signal intensity, as a pair of nickel dots are raster scanned through the micro-focused X-ray beam is shown in Fig. 5a. The FWHM vertical and horizontal micro-focused X-ray spot size was 6 and 24 μ m (17 μ m for normal incidence), respectively (Figs. 5c and d). Also shown is a normalized EXAFS scan on a single nickel dot, together with the k^2 -weighted χ spectrum (Fig. 6e). These data are reasonably good (collection time was 10 s per point), although there is a glitch in the data just below $k = 12 \text{\AA}^{-1}$ from the monochromator crystals. Fig. 6 shows a ray-tracing simulation of the focused spot size using the SHADOW ray-tracing code [15]. The ray-traced focused X-ray beam size for perfect KB optics is 5.85 μ m [vertical] \times 18.31 μ m [horizontal]. The experimental measurements agree very well with these values and small discrepancies between them are probably due to errors in the measured horizontal angle of the sample, the given electron source size parameters and figure errors of the mirror surfaces.

5. Mapping of Selenium on calcite growth surfaces

One important application at X27A is mapping distributions of minor and trace elements associated with environmental and geological materials, especially minerals. Low element concentrations and heterogeneous micro-spatial distributions pose challenges for characterization. During preliminary testing at X27A, we examined the spatial heterogeneity of SeO_4^{2-} incorporation into the common mineral calcite (CaCO_3) during low-temperature solution growth. Prior studies have shown that the (10 $\bar{1}$ 4) surface of this mineral grows by the spiral mechanism, producing polygonized growth hillocks composed of two pairs of vicinal faces (labelled + and – in Fig. 7a) that differ in the orientation and structure of their monolayer growth steps. Divalent cations, substituting at Ca^{2+} sites, have been shown to be incorporated differently between the

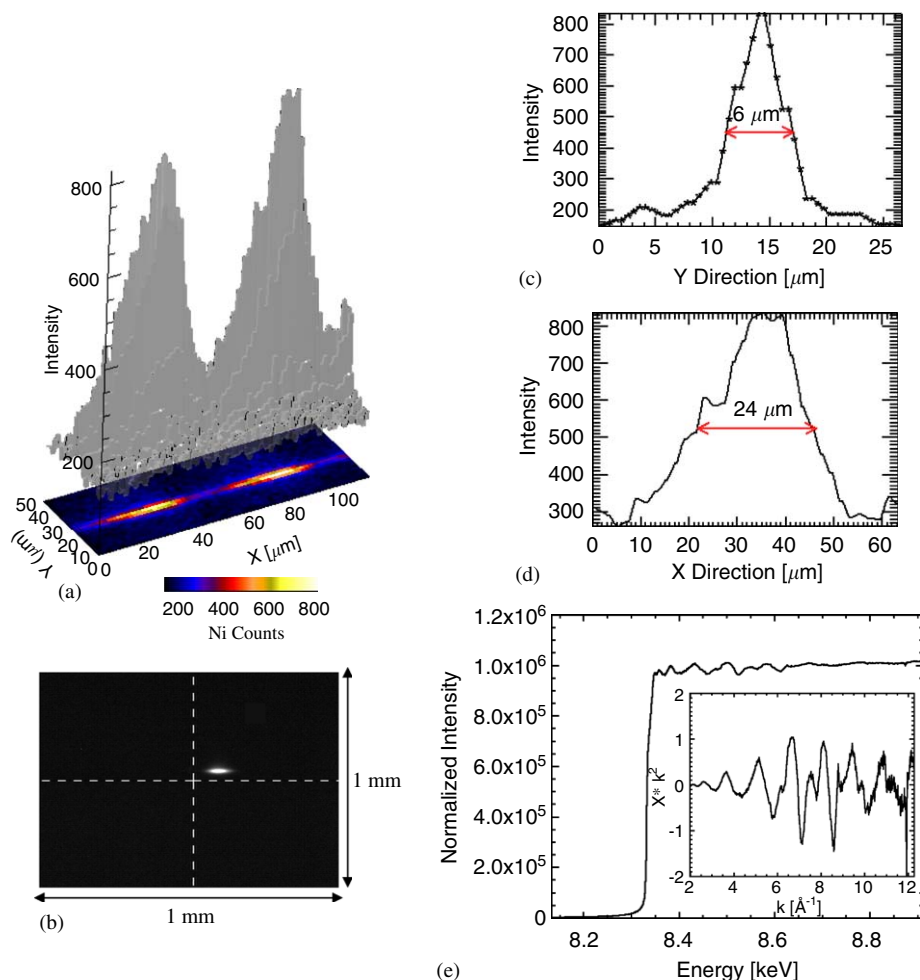


Fig. 5. (a) Nickel $K\alpha$ fluorescence image of a pair of 1500 \AA thick Ni dots evaporated on a silicon substrate. (b) Optical image of the X27A micro-focused X-ray beam using a scintillator crystal—the field of view was $1 \text{ mm} \times 1 \text{ mm}$ and the magnification was 10x. (c) Intensity profile along the center of a Ni dot in the y (vertical) direction. (d) Intensity profile along the center of a Ni dot in the x (horizontal) direction. (e) Normalized EXAFS spectra from a single nickel dot and the associated k^2 -weighted χ -spectra. A data collection time of 10 s per energy point was used.

nonequivalent vicinal surfaces as a result of different preferences for coordination at nonequivalent growth steps [16]. An earlier study indicated that the oxyanion selenate (SeO_4^{2-}) is also differentially incorporated at the calcite surface [17]. In this example we have used the micro X-ray fluorescence capability of X27A to map the Se distribution over the $(10\bar{1}4)$ surface of a $\sim 300 \mu\text{m} \times 300 \mu\text{m}$ ($\times 40 \mu\text{m}$ thick) CaCO_3 single crystal. Fig. 7b shows the Se distribution (Se $K\alpha$ counts) for the crystal shown in Fig. 7a, obtained from an 11 h scan, at an incident energy of 14 keV, and with a dwell time of 30 s per pixel. The correspondence of highest Se concentration with the + vicinal surfaces is clearly evident, whereas the vicinals are uniformly depleted in Se. The circular, Se-poor region at top-right corresponds to a small region with a different step structure. The Se map can be compared to the corresponding Ca map (Fig. 7c) which lacks the spatial distribution pattern of the Se, but does show a common artifact resulting from the 45° incident beam angle. The edge of a thin section facing the beam shows higher counts, whereas the edge facing away from the beam shows lower counts,

resulting in an apparent gradient in the Ca concentration, an effect that can also result from a wedge-shaped section.

Absolute Se concentrations were determined at four positions (A, B, C and D in Fig. 7b) using counts collected for 300 s. A standard-less, fundamental parameters approach was used to quantify the Se abundance using a modified version of the public-domain software NRLXRF [18], as described by Lu et al. [19], yielding 77, 64, 23 and 22 ppm Se at locations A, B, C, and D, respectively. A XANES spectrum taken at location A is shown in Fig. 7d and has been used to confirm the oxidation state of Se as $6+$.

6. Summary

In this paper, we report the design and performance of the new hard-X-ray micro-spectroscopy facility at bending-magnet beamline NSLS X27A. The performance of this new beamline and end-station closely matches expected operational parameters in spatial and energy resolution, intensity and stability, after recently undergoing a thorough commissioning cycle. A sample of research studies

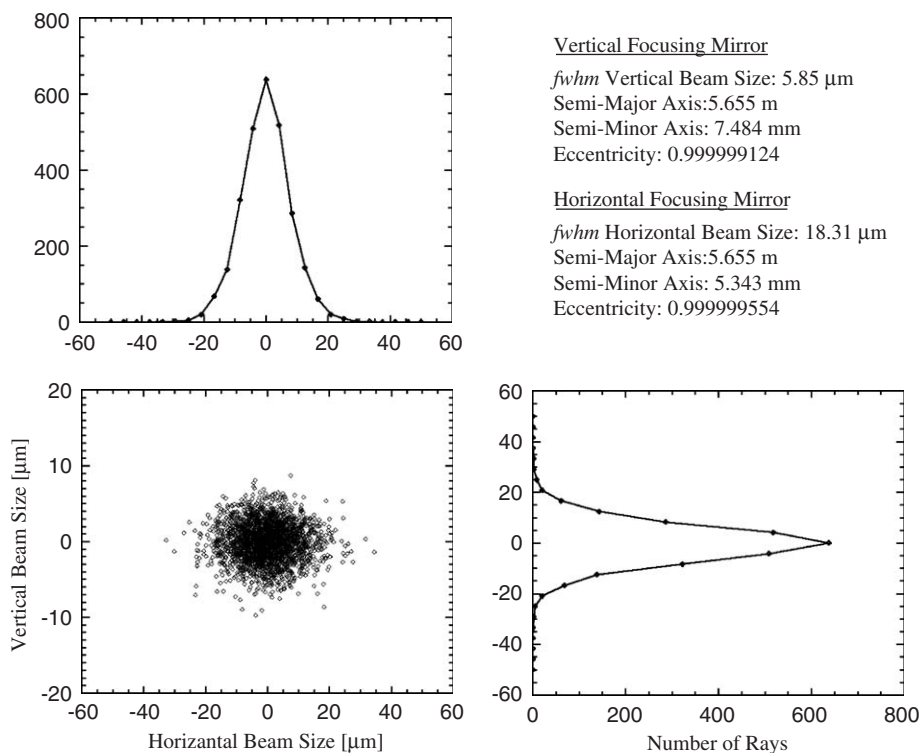


Fig. 6. SHADOW ray-tracing simulation of the focused beam size at X27A using ideal optics. The perfect focused X-ray beam size is (FWHM) 5.85 μm [vertical] \times 18.31 μm [horizontal].

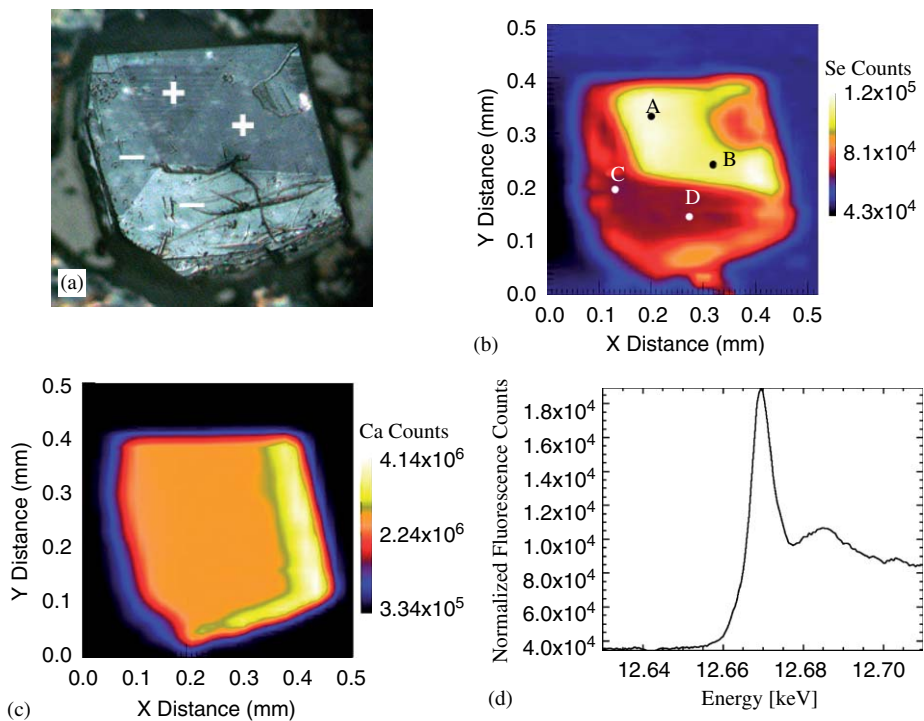


Fig. 7. (a) Optical differential interference contrast image of a $\sim 300 \mu\text{m} \times 300 \mu\text{m}$ ($\times 40 \mu\text{m}$ thick) calcite crystal used in the investigation of SeO_4^{2-} incorporation into CaCO_3 . Spatial distribution of selenium (b) and calcium (c) obtained by raster scanning the crystal through the X27A micro-focused X-ray beam and collecting and discriminating the characteristic fluorescence X-rays. (d) XANES spectrum taken at the selenium K-edge at position A in Fig. 7b.

recently performed at the beamline include the fluorescence mapping of heavy metals in diseased bone and brain, EXAFS measurements on patterned thin-film diffusion barriers, XANES on heavy metal contaminants in a wide range of environmental systems (roots, leaves, sediments and soils) and on systems under ultra-high pressure within a diamond-anvil cell. In the future, upgrades to the X27A micro-spectroscopy facility will be performed, including the implementation of X-ray Laue micro-diffraction and fluorescence micro-tomography methods. By providing the ability of characterizing a sample's microstructure and internal elemental distributions, these techniques will be powerful additions to the micro-spectroscopy capabilities at X27A, a resource that is already proving to be a valuable component of microprobe research at the NSLS.

Acknowledgements

Research carried out at the National Synchrotron Light Source, Brookhaven National Laboratory, which is supported by the US Department of Energy, Division of Materials Sciences and Division of Chemical Sciences, under Contract no. DE-AC02-98CH10886. The Center for Environmental Molecular Science (CEMS) at Stony Brook University contributed to initial planning and design for this new facility. We gratefully acknowledge Christopher Stelmach, Sal Pjerov, Anthony Lenhard, Shu Cheung, James Newburgh, Richard Green and Zhijian Yin at the National Synchrotron Light Source for their hard work and dedication throughout this project. We also acknowl-

edge valuable scientific input from Professor Chris Jacobsen at the University of New York at Stony Brook, and Dr. Jeffrey Fitts, Dr. Paul Northrup and Dr. Mark Fuhrmann of the BNL Environmental Sciences Department. Finally, we would like to thank Dr. Peter Eng and Dr. Mark Rivers at the University of Chicago, for valuable insight and advice in implementing the micro-focusing X-ray optics and beamline control system at X27A.

References

- [1] G.E. Ice, *X-Ray Spectrom* 26 (1997) 315.
- [2] P. Dhez, et al., *Rev. Sci. Instrum.* 70 (1999) 1907.
- [3] J. D'Amore, et al., *J. Environ.Qual.* 34 (2005) 1707.
- [4] K.G. Scheckel, et al., *Environ. Sci. Technol.* 38 (2004) 5095.
- [5] G. Sarret, et al., *Environ. Sci. Technol.* 38 (2004) 2792.
- [6] D.G. Schulze, et al., *Phytopathology* 85 (1995) 990.
- [7] P.M. Bertsch, D.B. Hunter, *Chem. Rev.* 101 (2001) 1809.
- [8] A. Manceau, M.A. Marcus, N. Tamura, *Rev. Mineral. Geochem.* 49 (2002) 431.
- [9] S.R. Sutton, et al., *Rev. Sci. Mineral. Geochem.* 49 (2002) 429.
- [10] D.P. Siddons, *Proc. SPIE* 3151 (1997) 230.
- [11] L.E. Berman, et al., *Rev. Sci. Instrum.* 73 (2002) 1481.
- [12] M.O. Krause, J.H. Oliver, *J. Phys. Chem. Ref. Data* 8 (1979) 329.
- [13] M.O. Krause, *J. Phys. Chem. Ref. Data* 8 (1979) 307.
- [14] B.X. Yang, et al., *Rev. Sci. Instrum.* 66 (1995) 2278.
- [15] C. Welnak, et al., *Rev. Sci. Instrum.* 63 (1992) 865.
- [16] E.J. Elzinga, R.J. Reeder, *Geochim. Cosmochim. Acta* 66 (2002) 3943.
- [17] W.J. Staudt, R.J. Reeder, M.A.A. Schoonen, *Geochim. Cosmochim. Acta* 58 (1994) 2087.
- [18] J.W. Kriss, L.S. Birks, J.V. Gilfrich, *Anal. Chem.* 50 (1978) 33.
- [19] F.Q. Lu, et al., *Chem. Geol.* 75 (1989) 123.